Evaluation of Carbon Partitioning in New Generation of Quench and Partitioning (Q&P) Steels

Ariza, E. A.[a]*; Babu, S. S.[b]; Poplawsky J. D.[c]; Guo, W. [c]; Unocic K. A.[d], Ramirez, A. J.[e]; Tschiptschin, A. P.[a]

[a] Department of Metallurgical and Materials Engineering, University of São Paulo, Av. Prof. Mello Moraes, 2463, São Paulo-SP, Brazil, 05508-030

[b] Department of Mechanical, Aerospace and Biomedical Engineering, The University of Tennessee, Knoxville-TN, 37996-2210, USA

[c] Center for Nanophase Materials Sciences, Oak Ridge National Laboratory, P.O. Box 2008, Oak Ridge-TN 37831-6064, USA

[d] Materials Science and Technology Division, Oak Ridge National Laboratory, P.O. Box 2008, Oak Ridge-TN 37831-6139, USA

[e] Department of Materials Science and Engineering, Ohio State University, Columbus-OH, 43221, USA.

* Corresponding authors: e-mail: andersonariza@usp.br

Abstract

Quenching and partitioning (Q&P) and a novel combined process of hot straining (HS) and Q&P (HSQ&P) treatments have been applied to a TRIP-assisted steel in a Gleeble®3S50 thermo-mechanical simulator. The heat treatments involved intercritical annealing at 800 ºC and a two-step Q&P heat treatment with a partitioning time of 100 s at 400 °C. The "optimum" quench temperature of 318 ºC was selected according to the constrained carbon equilibrium (CCE) criterion. The effects of high temperature deformation (isothermal and non-isothermal) on the carbon enrichment of austenite, carbide formation and the strain-induced transformation to ferrite (SIT) mechanism were investigated. Carbon partitioning from supersaturated martensite into austenite and carbide precipitation were confirmed by means of atom probe tomography (APT) and scanning transmission electron microscopy (STEM). Austenite carbon enrichment was clearly observed in all specimens, and in the HSQ&P samples it was significantly greater than in Q&P, suggesting an additional carbon partitioning to austenite from ferrite formed

by the deformation induced ferrite transformation (DIFT) phenomenon. By APT, the carbon accumulation at austenite/martensite interfaces was observed, with higher values for HSQ&P deformed isothermally (≈ 11 at.%), when compared with non-isothermal HSQ&P (≈ 9.45 at.%) and Q&P (≈ 7.6 at.%). Moreover, a local Mn enrichment was observed in a ferrite/austenite interface, indicating ferrite growth under local equilibrium with negligible partitioning (LENP).

1. Introduction

Carbon in retained austenite is considered to be the chemical element that controls its stability at room temperature and the plasticity of the material, especially in low alloy steels [1]. However, in TRIP steels, research has shown that the stability of the retained austenite is affected not only by the carbon [2,3] or manganese content [4,5], but also by its distribution, morphology and grain size [6,7]. The constraints imposed by the phases surrounding the austenitic phase [8], and the crystallographic orientation of the austenite, with respect to the loading direction (Schmid factor), also influences the stability of retained austenite [9,10]. With regard to the dependence of the grain morphology on the carbon content of retained austenite, there is a notable discrepancy in the literature. Some authors report that austenite in the form of films has a higher carbon content [11–13], while others assert the opposite, that austenite in the form of blocks has shown a higher carbon content [14,15]. However, all these authors concur that austenite retained in the form of films is more stable against mechanical deformation, even when having a lower carbon content. This behavior is mainly associated with the greater number of defects, such as stacking faults or dislocations, present in austenite in the form of blocks [12], which act as martensite nucleation sites, even at low deformations. Furthermore, interlath retained austenite films are generally surrounded by microconstituents with greater hardness and strength to plastic flow, such as martensite and bainite. Thus, the austenite is stabilized by the high hydrostatic pressure exerted by these phases, which restricts the volumetric expansion and the shear strain associated with the martensitic transformation [12,16]. Hence, since the retained austenite's stability and the carbon distribution are assumed to be the key parameters that influence the phase transformation and mechanical

properties, the characterization and understanding of carbon enrichment and the volume fraction of retained austenite are important.

The underlying principle of the "quenching and partitioning" (Q&P) process [17] is the transfer of carbon from the supersaturated martensite to the austenite. In the Q&P process, the steel is austenitized (either fully or partially) and then quenched to a temperature between the martensite start (M_s) and martensite finish (M_f) temperatures to create a controlled mixture of martensite and austenite (and any intercritical ferrite present during annealing). The steel is then isothermally held (annealing treatment or ageing, commonly termed the partitioning step) at the same quenching temperature (T_Q) (one-step Q&P treatment) or heated to a higher temperature (T_P) than T_Q (two-step Q&P treatment). The martensite carbon content at T_Q is equal to the bulk carbon content in samples quenched from austenite, and is greater than the bulk carbon content in samples intercritically annealed prior to quenching [18]. During a subsequent isothermal holding (partitioning stage), the carbon can diffuse from the supersaturated athermal martensite into the remaining untransformed austenite, stabilizing this phase during the final quench to room temperature. It has been suggested that this carbon partitioning is controlled by the constrained carbon equilibrium (CCE) criterion [17], which assumes an identical chemical potential of carbon (not applicable to substitutional solutes) in each phase, a stationary austenite/martensite interface, and that no competing reactions occur, such as carbide precipitation.

Carbon-enriched austenite stabilized at room temperature has the ability to contribute to mechanical properties in the same way that it does in TRIP-assisted steels [19]. Moreover, the enriched carbon concentration also increases the strength of the partitioned untransformed austenite [20]. For this reason, the subject of Q&P has been extensively studied during the past few years [21–24]. Liu et al. [25] indicated that while the Q&P process is one of the most likely methods for producing AHSS with high strength and elongation, the heat treatment methods do not take into account the strain-induced phase transformations. Some studies have investigated the possibility of using a combination of the quenching and partitioning with the hot stamping process [25–30]. Furthermore, those studies only used isothermal straining and one-step Q&P condition in samples fully austenitized, with the exception of Ariza et al.

[30] and Chang et al. [27]. However, Chang et al. [27] implemented a two-step Q&P process, with one minute of quenching time before the partitioning treatment, which is a longer period of time than was suggested by De Knijf et al. [31], since it can cause the precipitation of isothermal transformation products.

Atom probe tomography (APT) has emerged as a unique technique that is able to provide information about the three-dimensional distribution of elements with nanoscale resolution. Some authors [18,23,32–34] carried out APT measurements to obtain information on the amount and location of carbon within Q&P microstructures. However, there is still not enough information on the carbon enrichment of austenite in the Q&P treatment after deformation at high temperatures (henceforth referred to as HSQ&P). Hence, the APT technique is able to clarify whether the DIFT (deformation-induced ferrite transformation) effect [35] or the strain-induced transformation to ferrite (SITF) mechanism [36] contribute to the enrichment of austenite and its stabilization and whether carbide precipitation concomitant with ferrite precipitation hinders the diffusion of carbon to neighboring austenite.

In this study, a novel combined process of hot straining, using an isothermal and a non-isothermal deformation and intercritical annealing, followed by a two-step Q&P treatment (HSQ&P) applied to TRIP-assisted steel, has been conducted. The aim is to compare the Q&P process with the same process when previous hot deformation is included. In order to understand the role of the partitioning stage on the distribution (or segregation) of the solute (carbon and substitutional elements) in the retained austenite, ferrite, martensite and the tempering reactions that may occur (such as carbide precipitation or carbon atom clustering at the dislocations or at the interfaces), with a special focus on the carbon and manganese profiles, the samples were analyzed by APT in regions identified as austenite (both block and film), ferrite, martensite, interfaces and carbides. The understanding of carbon redistribution during the Q&P and HSQ&P processes is important for the development of complex microstructures in advanced high-strength steels.

2. Experimental Procedures

A commercial TRIP-assisted steel (Fe–0.23C–1.23Si–1.50Mn, wt.%) was subjected to Q&P and HSQ&P experiments. A Gleeble®3S50 thermomechanical simulator was used to reproduce the thermo-mechanical treatment conditions, as schematically depicted in Fig. 1. The as-received multiphase specimens (bainite, ferrite, martensite, and retained austenite) were heated up to 1000 °C at a rate of 15 °C/s, held for 5 min so as to become homogeneous, and then intercritically annealed at 800 °C for 5 min. For the HSQ&P processes, after intercritical annealing, the samples were strained. The magnitude of the applied true strain was 0.3 and the initial deformation temperatures were 750 °C (a non-isothermal process, where the sample is cooled down while being simultaneously deformed) and 800°C (an isothermal process) (Fig. 1b and 1c). The nominal strain rate in both cases was 0.5 s^{-1}, which is within the range of strain rates encountered during a conventional hot stamping [37] process. The strain was controlled using a non-contact laser dilatometer that provided real-time measurements of the sample width. The test temperature was monitored using a thermocouple welded on the center of the specimen surface. The optimum quenching temperature (QT), which gives the maximum retained austenite fraction at room temperature at the end of a Q&P process, was estimated according to the constrained carbon equilibrium (CCE) model [17] and based upon the Koistinen and Marburger equation empirically determined in a previous quenching experiment [30]. Therefore, the samples were quenched at 318 °C (QT) for 5 s, reheated at 15 °C/s to 400 °C and held for 100 s for the partitioning step, and then finally cooled down to room temperature. The cooling rate during the quenching steps was kept at 60 °C/s.

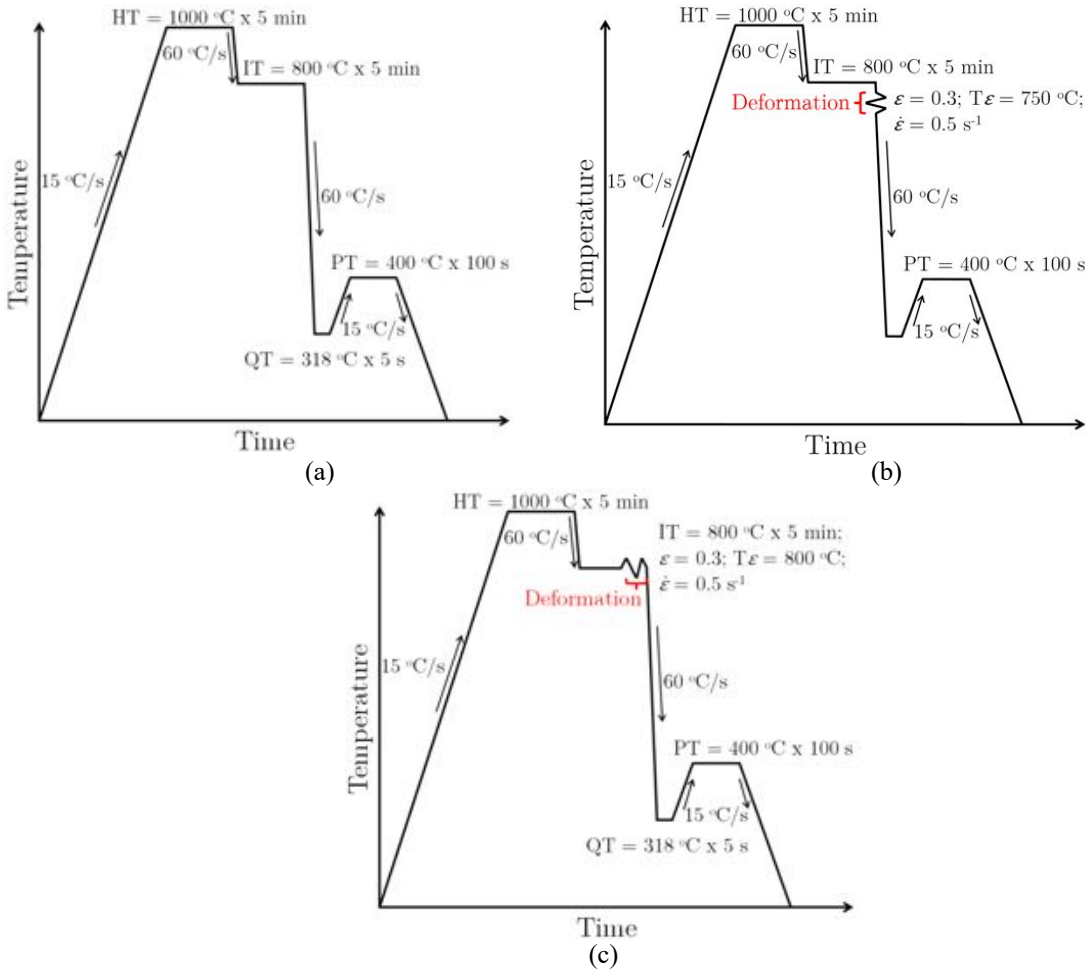

Fig. 1. Schematics of the HSQ&P thermomechanical treatments: (a) Q&P; (b) HSQ&P, with initial deformation temperature at 750 °C; (c) HSQ&P, with initial deformation temperature at 800 °C. HT, IT, QT, and PT are homogenization, intercritical, quenching, and partitioning temperatures, respectively.

Electron back-scattered diffraction (EBSD) analyses were carried out using an acceleration voltage of 20 keV, a specimen tilt angle of 70° with 15 mm working distance, and a scan step size of 0.1 μm. In order to provide direct evidence that certain regions in the APT and TEM data are indeed austenite, ferrite and/or martensite, phase identification by combining EBSD and nanoindentation marks was used. Hence, EBSD and nanoindentation tests (which leave distinct markings that are easy to identify but at the same time do not cause high stress concentrations) can be used to find particular microconstituents and interfaces of interest in complex microstructures for further analysis with APT or TEM. Nanoindentation tests were carried out using the Triboindenter TI 950 (Hysitron Inc.) in load control testing mode at a constant strain rate

($\dot{\varepsilon} = \dot{h}/h$) of 0.42 s^{-1}, where h is the penetration depth and $\dot{h}$ is the penetration rate of the indenter.

The identification of phases was carried out through the correlation of nanoindentation values, image quality (IQ), and kernel average misorientation (KAM), as shown in Fig. 2. The IQ parameter facilitates to distinguish microstructural constituents by the degree of lattice imperfection [38,39]. This is because a lattice distorted by crystalline defects such as high dislocation densities, lattice strain, and grain or sub-grain boundaries will have a deformed arrangement of the Kikuchi Pattern, leading to lower IQ values [38,39]. The orientation data acquired by EBSD scan can also be used to investigate the local strain distribution among different grains, that is important to identify the orientation gradients physically associated with dislocation glide and crystal lattice rotation [40,41]. The KAM distribution map, which represents the arithmetic average misorientation between a point in the center of a pre-determined kernel and the points in the perimeter of the kernel [39], was used to evaluate qualitatively small local strain gradients or localized plastic strain distribution among different grains [40].

The IQ combined with phase identification was used to distinguish face-centered cubic (FCC) and body-centered cubic (BCC) phases and IQ combined with KAM (calculated for the 5^{th} nearest neighbors of each point and upper limit of 10º) was used to distinguish the BCC ferrite and martensite areas. The gray color in Fig. 2a corresponds to the BCC crystal structure, and the red corresponds to FCC lattice (retained austenite). It is known that the martensite have a higher degree of lattice distortion (tetragonal distortion related to its carbon content [42]) and a larger density of subgrain boundaries [38]. Hence, the higher values of hardness (ranged from 5.1 to 6.8 GPa) match the darker areas, which indicate lower IQ (or band contrast, BC) and high dislocation density. In Fig. 2b, the blue color displays misorientations less than 2º, green between 2º and 4º, yellow between 4º and 6º, orange between 6º and 8º and red between 8º and 10º. This figure indicates that the highest values of KAM are present in locations of greater lattice deformation (i.e., areas of martensite) and the lowest KAM values correspond to ferrite grains with higher BC. Consequently, the correlation between the high dislocation densities and the low image quality is evident [38], which can be confirmed by high nanohardness values. Accordingly, the differentiation of IQ and KAM distributions

caused by the lattice imperfection can be readily used to identify the orientation gradients and for discrimination among ferrite and untempered and fresh martensites in the TRIP-assisted steel [43].

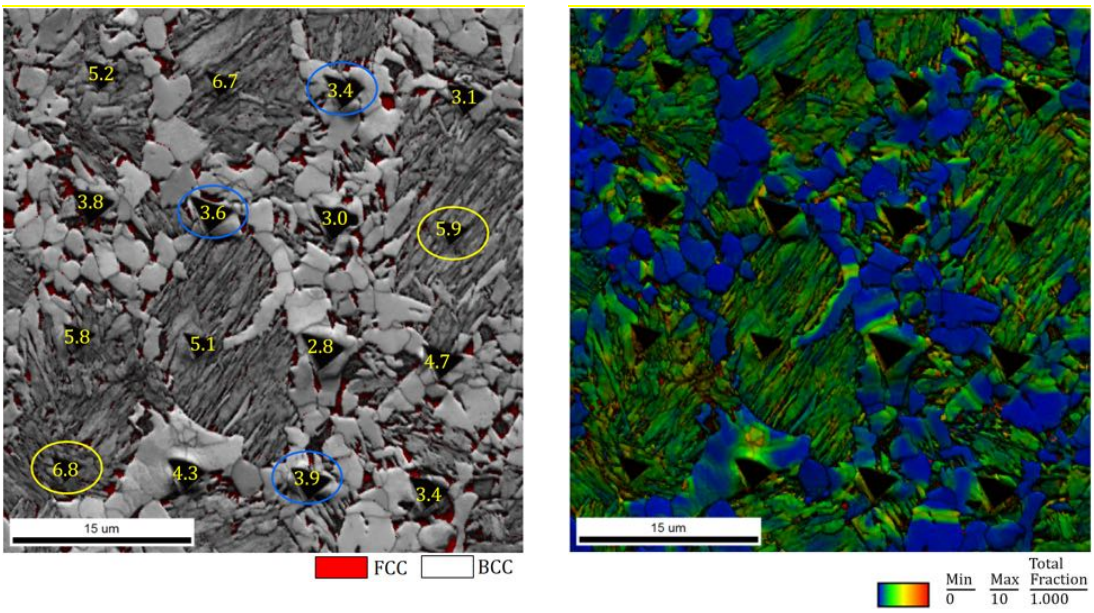

(a) (b)

Fig. 2. Identification of phases through nanoindentation, image quality (IQ), and kernel average misorientation (KAM) in the HSQ&P$_{800}$ processed TRIP-assisted steel. (a) Combined IQ map and color coded phase map. Blue and yellow circles indicate ferrite and martensite regions, respectively. (b) KAM map calculated with the 5th nearest neighbors of each point and upper limit of 10º. Nanohardness values in GPa.

In this work, the mechanical properties obtained through nanoindentation tests are not discussed, since this methodology has already been done, for Q&P and HSQ&P processes applied to TRIP-assisted steel, in a recently published study by Ariza et al. [30]. After EBSD/nanoindentation identification, APT was applied for the near-atomic quantitative investigation of carbon partitioning in the Q&P and HSQ&P processed TRIP-assisted steel. For APT analysis, site-specific focused ion beam (FIB) lift-outs were taken from regions with a high density of austenite and martensite interfaces. Several sections of the lift-out were mounted on a micro-tip array and each was annularly milled (acceleration voltage of 30 kV) and cleaned (5 kV) with an ion beam to make needle-shaped specimens suitable for field evaporation [44]. APT of the resulting needle-shaped specimens was

performed using a CAMECA Instruments LEAP® 4000X HR local electrode atom probe, which is equipped with an energy-compensating reflectron lens for improved mass resolution. The specimens were field evaporated in laser mode with a 200 kHz pulse repetition rate at the temperature of 30 K, 50 pJ laser power, and a 0.5–1.0% detection rate. The resulting data were reconstructed and analyzed using the CAMECA IVAS software. Gallium damage from the FIB-based specimen preparation method was assessed and removed using the Ga^{+} and Ga^{++} isotopes, which was minimized by the 5 kV cleaning step. Deconvolution of the ions within overlapping isobars of different elements (e.g., Cr54/Fe54 and C_2^{+}/C_4^{++}) was performed based on the natural abundances of the elements.

Specimens were examined by scanning transmission electron microscopy (STEM) using a FEI Talos F200X microscope operated at 200 kV and equipped with an extreme field emission gun (X-FEG) electron source and Super-X EDS (energy dispersive spectroscopy) system with 4 silicon drift detectors (SDD) for chemical analysis. APT and STEM specimens were prepared via the focused ion beam (FIB) milling technique by the in-situ lift-out method using a Hitachi NB5000 FIB-SEM.

3. Results and Discussion

3.1 Characterization of the Q&P sample

Due to the microstructural complexity of the samples after the Q&P and HSQ&P treatments, the results obtained by EBSD and nanoindentation were used to identify the phases, microconstituents, and grain boundaries of interest for further analysis by APT, as shown in Fig. 3, for the Q&P sample quenched at 318 °C and partitioned at 400 °C for 100 s. In this figure, the size and distribution of austenite (FCC lattice) are indicated by the red areas, while the ferrite and martensite phases (BCC lattice) appear gray. This methodology for localization of regions or microconstituents proved to be efficient to be applied in complex microstructures that will later be analyzed by APT or STEM. As expected from the difference in dislocation densities of martensite and ferrite (BCC lattice), two distinct image quality regions are observed in the combined IQ and color-coded phase map (Fig. 3a) and in the KAM map (Fig. 3b). As state above, the largest

lattice defect density in martensite causes a decrease in IQ compared to that of ferrite regions [42], which enables to identify polygonal ferrite being the light area with high IQ and low KAM and martensite being the dark area with low IQ and a considerable higher degree of local misorientation. In Fig. 3a, it is possible to observe the (two) regions identified for extraction of the lamellae for the APT analysis. In region 1, our interest was to study the concentration of carbon in a ferrite/austenite interface (α/γ, austenite in red), while in region 2, the aim was to quantify the carbon content of a fine retained austenite film (γ_f) between the martensite (α') plates.

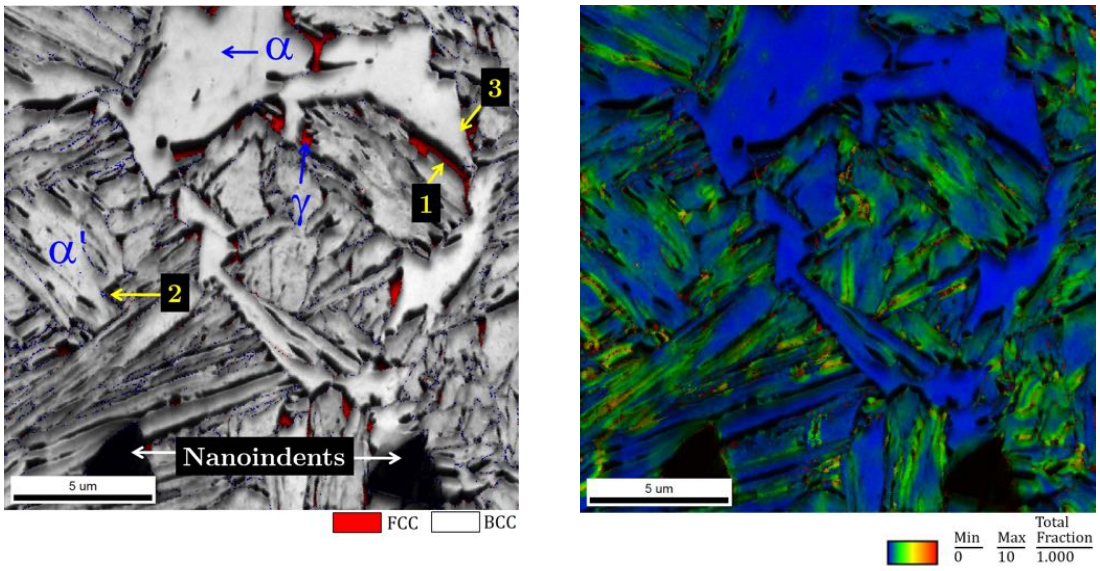

(a) (b)

Fig. 3. EBSD phase map and nanoindentations of the Q&P sample, austenitized at 800 °C quenched at 318 °C, and partitioned at 400 °C for 100 s. (a) Combined IQ map and color coded phase map, (b) KAM map.

Fig. 4 shows the APT results of the regions identified with numbers 1 and 2 in Fig. 3. Fig. 4a shows the carbon atom map of a block-form austenite, containing approximately 6.00 at.% C, extracted from a region between a ferrite grain and a martensite region ($\alpha/\gamma_b/\alpha'$). The carbon content of this retained austenite is considerably higher than the nominal carbon content of the material (1.06 at.% C). This result is close to that recently determined by Poling et al. [45] (≈ 5.7 at.%), which was also obtained for a block-form retained austenite in a steel subjected to the Q&P process. Poling et al. [45] pointed out that they made several attempts to analyze other regions which included austenite in the

form of films, but the attempts were unsuccessful. In Fig. 4b the APT results of the sample extracted from region 2 are shown. In this figure, it is possible to distinguish martensite with an average carbon content of approximately 0.23 at.%, a film-type retained austenite (γ_f) with approximately 5.51 at.% C, and precipitates in martensite with approximately 25 at.% C, which is most probably cementite (θ, Fe_3C), with the corresponding stoichiometric carbon concentration. These precipitates were most likely formed during tempering of as-quenched martensite at 400 °C. The atomic fractions of carbon, manganese, and silicon using proximity histograms were estimated by means of isoconcentration surfaces at 2 at.%. The concentration profiles of the substitutional elements indicate that there was no partition of manganese and silicon between martensite and austenite, so that only the carbon partition occurred during the partition stage at 400 °C for 100 s. On the other hand, the silicon behavior in the composition profile of the θ precipitate (bottom part in Fig. 4b) is compatible with the formation of cementite, since it is well known that due to the low solubility of the silicon in the cementite, its growth must be accompanied by rejection of silicon. The constrained carbon equilibrium (CCE) criterion assumes that all carbon is partitioning from martensite to austenite during the partition stage. Thus, the formation of tempered carbides (such as cementite) is one of the mechanisms that cause a significant deviation of the model, reducing the potential for the carbon enrichment of austenite. The presence of cementite in the martensite, evidenced in the APT measurements, clearly indicates that the suppression of carbide precipitation considered in the CCE model is not necessarily true, even for steels containing silicon (1.23 wt.%). However, the reaction is markedly retarded to allow significant carbon enrichment in the austenite during the partitioning process and then it enhances the stability of the remaining austenite.

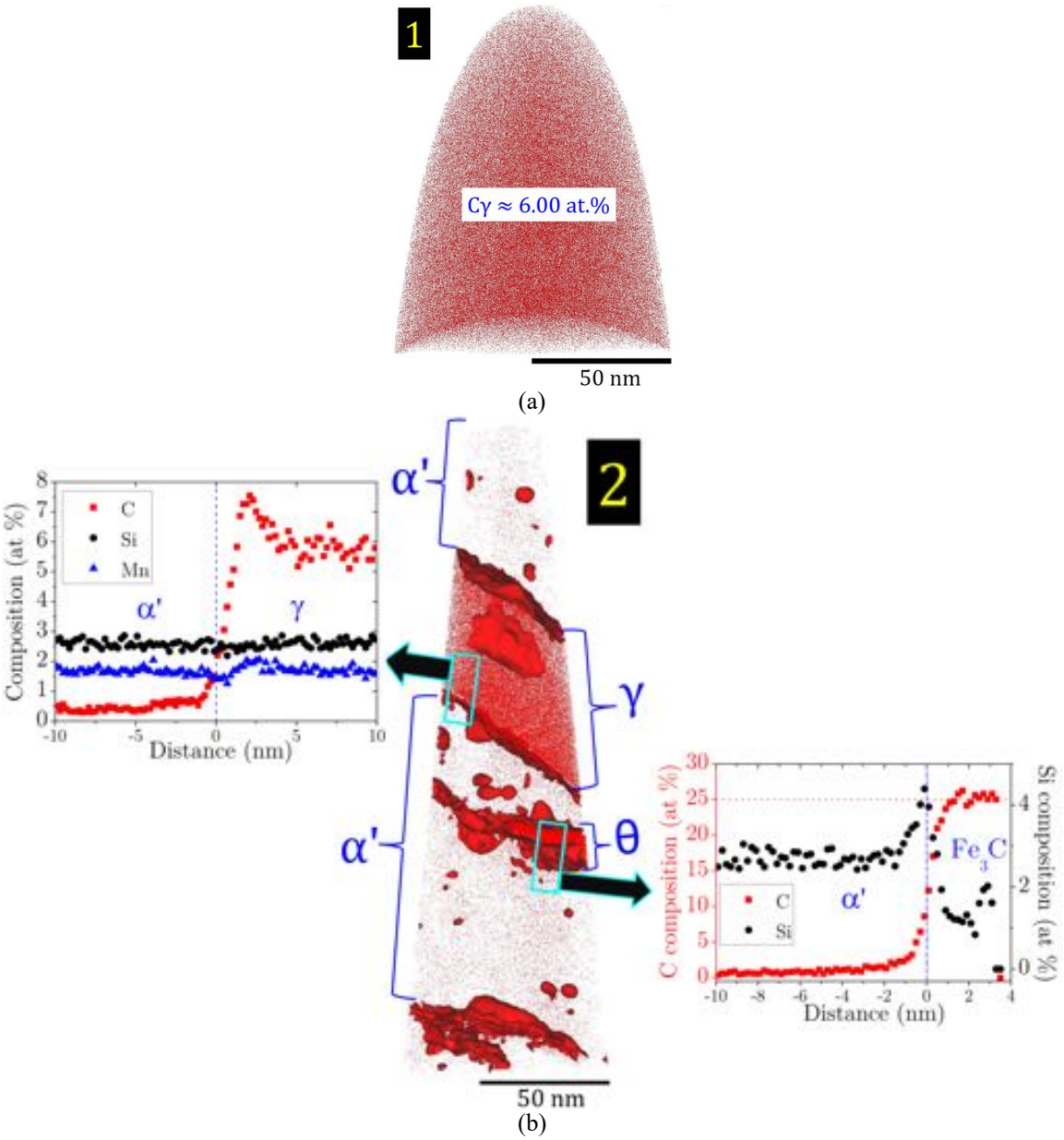

Fig. 4. (a) Carbon atoms map of a block-form austenite, containing approximately 6.00 at.% C, from the region identified by the number 1 in Fig. 3. (b) Carbon isoconcentration surfaces at 2 at%. C superimposed with the carbon atom map (center), for a needle extracted from region 2 in Fig. 3, and proximity histograms obtained across the martensite (α')/austenite (γ) interface (left) and through a cementite (θ or Fe_3C)/α' interface (right). The small green boxes show the regions through a carbon cluster and the interface (α'/γ) selected, for carbon, silicon, and manganese concentrations analysis.

The carbon partitioning evidenced in the proxigrams (histograms of the composition profiles) allows for the identification of phases and grain boundaries. The green boxes in

Fig. 4 indicate the volumes along which the concentration profiles were measured. In the bottom proxigram the concentration profiles of atoms of carbon, manganese, and silicon are presented, starting in martensite (α') and ending in austenite (γ). From this result, it is possible to observe that austenite is significantly enriched in carbon ($C\gamma_f \approx 5.51$ at.% C), while the martensite is depleted in carbon ($C\alpha' \approx 0.23$ at.%) with respect to the nominal carbon concentration of the steel (1.06 at.% C). In addition, at the α'/γ interface there is a carbon accumulation of approximately 7.6 at.% C, implying a negative carbon gradient in the austenite. These results are a strong evidence of the carbon partitioning from martensite to austenite during the partition stage. This phenomenon occurs because the chemical potential of carbon at the interface in supersaturated ferrite (α') is higher than in austenite and both phases have different solubilities. During the partitioning stage, the system aims to balance the chemical potential of carbon, giving rise to a carbon diffusive flux from martensite to austenite. According to the CCE model, the carbon partitioning ends when the metastable equilibrium between ferrite (α') and austenite (γ) is reached, i.e., when the carbon redistribution (partitioning) reaches the point at which the chemical potential of carbon is equal through the α'/γ interface. Thus, the evidence of a carbon concentration gradient at the interface might indicate that the carbon partitioning has not yet reached the steady state.

Estimation of the average time required (t) for the complete homogenization of carbon in the retained austenite from the martensite carbon migration can be obtained by Eq. (1):

$$t = \frac{\bar{x}}{6D} \tag{1}$$

with $\bar{x}$ and D denoting the average diffusion distance and the diffusivity of carbon in austenite, which can be expressed as:

$$D = D_0 \exp(Q / RT) \tag{2}$$

where D_0 is the pre-exponential constant (1.00×10^{-5} m^2/s), Q is the activation energy for diffusion of carbon in austenite (135.7 kJ/mol), R is the universal gas constant (8.314

J/K·mol), and T is the absolute temperature (K). For the calculations of the homogenization time, it is assumed that the average diffusion distance is equivalent to the austenite film thickness, i.e., ≈ 50 nm, according to Fig. 4. Application of Eq. (1) leads to a homogenization time, at the quench temperature (318 °C), of 41.4 s, while the holding time at that temperature was only 5 s. De Knijf et al. [46] pointed out that the isothermal holding time at the quenching temperature in Q&P steels needs to be kept short (usually five to ten seconds) in order to avoid the precipitation of isothermal transformation products at the quenching temperature. The same type of calculation applied at the partitioning temperature (400 °C) leads to a partition time of ≈ 1.43 s for complete homogenization of carbon in austenite. However, as shown in Figs. 3 and 4a, there are regions of austenite (blocky) up to 0.5 μm thick, for which a homogenization time of 142.9 s during the partitioning stage is required.

With regard to the effect of the austenite morphology on the carbon content, the retained austenite in blocky-type (γ_b) presents a higher concentration of carbon in relation to austenite in the film-type (γ_f): $C\gamma_b \approx 6.00 \pm 0.01$ at.% and $C\gamma_f \approx 5.51 \pm 0.02$ at.%. This can be explained by the contribution of carbon enrichment (in blocky austenite) of both ferrite and martensite. In addition, the cementite formation observed in martensite in the vicinity of film-like austenite has a direct influence on the available carbon to be partitioned from martensite.

3.2 Characterization of the HSQ&P sample strained at 750 ºC

The APT results for the sample HSQ&P strained at 750 ºC in 30% (true strain) at a rate ($\dot{\varepsilon}$) of 0.5 s^{-1}, quenched at 318 °C and partitioned at 400 °C for 100 s, are presented in Fig. 5. In this figure, the size and distribution of austenite are indicated by the red areas, while the ferrite and martensite phases appear green. In Fig 5a and c, it is observed that the grains with higher subgrain boundaries always have relatively lower IQ values. Hence, owing to a less perfect BCC lattice, martensite can qualitatively be distinguished from ferrite by darker regions with a lower image quality based on the very high dislocation density of martensite [42,43,47]. This enables identifying martensite (α'), fresh martensite (α'_f), ferrite (α) and austenite (γ) in Fig 5. The yellow rectangles indicate

the regions from which the needles were extracted by FIB for further analysis by the APT.

Comparing the EBSD phase maps in Fig. 5 with that of the sample submitted to the Q&P treatment (Fig. 3), it is possible to observe how the high-temperature deformation promotes the reduction of the grain size of both ferrite and martensite, which could contribute to improve the strength-ductility balance of the studied TRIP-assisted steel. The decrease in the grain size can be attributed to a dynamic recovery process, in which, in the same sliding plane, the density of dislocations decreases through the mutual annihilation of dislocations of opposite sign.

The identification of the nanoindentation values in the EBSD images makes it possible to relate the values of nanohardness with the analyzed regions and, in this way, to identify the grains of ferrite, martensite, and austenite present in the analyzed volume. The map of the carbon atoms of an α/γ interface and its local composition profile by proximity histogram of carbon, silicon, and manganese are shown in Fig. 5b. The results of the composition profile showed a significant carbon enrichment in austenite ($C\gamma \approx 6.63 \pm 0.01$ at.%), while the results for silicon and manganese did not show an evident partitioning at the α/γ interface. In Fig. 5b, a carbon accumulation at the α/γ interface (≈ 9.45 at.%) was also observed. In order to analyze if there was a carbide precipitation into the martensite under the heat treatment conditions studied here, an APT measurement was conducted on a needle extracted from the region clearly delimited as martensite by the blue contour dotted in Fig. 5c, specifically at the region delimited by the yellow rectangle. Fig. 5d shows the composition profile of Si, C, and Mn at the interface of the cluster indicated by the blue arrow at the carbon isoconcentration surface at 7 at.% C superimposed with the carbon atom map. This result reveals that the Si concentration is homogeneous in both α' and the cluster, indicating that it is probably a preferential agglomeration of carbon atoms instead of a cementite particle. In addition, the cluster has a lower carbon content (≈ 15 at.%) than expected for a stable precipitate such as cementite (≈ 25 at%), or for transition carbides (metastable) such as ε-carbide (≈ 33 at.%), $Fe_{2,4}C$ (hexagonal) or the η-carbide (≈ 29 at%). Timokhina et al. [48,49] identified low-temperature carbides having carbon contents between 10 and 20 at.% in a dual-phase steel, such as $Fe_{32}C_4$ or $Fe_4C_{0.63}$. These carbides were associated with the

bainitic-ferrite formation during the isothermal transformation at low temperatures (≈ 200 °C), for long holding times (10 days), during the bake-hardening process and pre-strained to 5%. However, in the present study, the region where these clusters were identified was clearly identified by EBSD and nanoindentation as martensite. In addition, the low-carbon martensites consist of laths, separated by low or high-angle boundaries, but containing a high dislocation density between them [50]. It is known that grain boundaries and dislocations can act as sinks for carbon atoms due to the reduction of the chemical potential of carbon at these defects [51], which results in local carbon enrichment in these regions. Therefore, the clusters observed in Fig. 5d are likely to correspond with the carbon segregation at the boundaries of the martensite laths. It is important to note that the carbon clusters seem to align themselves in one single habit plane, or preferential invariant planes at the interface along which the martensite laths form. The characteristics of the parallel plates could correspond with the carbon segregation to stacking faults or microtwins in martensite, as observed by transmission microscopy (yellow arrows in Fig. 7). Another explanation is that this alignment could be caused by the applied stresses, which favor the formation of preferential crystallographic variants on the planes of the maximum shear stress planes [52]. Therefore, due to the fact that there are many crystallographic variants available per austenite grain, there is a high probability that the orientation of a plate is close to the preferred orientation for the alignment to occur with respect to the stresses [53]. It is worth noting that the presence of such agglomeration of carbon or the formation of precipitates in martensite reduces the levels of carbon available to enrich the austenite and stabilize it at room temperature.

Comparing the blocky-type austenite carbon contents (at an α/γ_b interface) of the HSQ&P sample strained at 750 ºC ($C\gamma_b \approx 6.63 \pm 0.01$ at.%) and the Q&P sample ($C\gamma_b \approx 6.00 \pm 0.01$ at.%), both quenched at 318 °C and partitioned at 400 °C for 100 s, it is possible to observe an increase of ≈ 10% in the carbon content for the HSQ&P sample. This result can be explained by the additional contribution (besides the portion of carbon depletion of the supersaturated martensite in the partitioning step) in the carbon enrichment of austenite produced by the partitioning of carbon from the ferrite formed during the straining at high temperature, i.e., formed by the DIFT effect [35,54]. This is a combined increase effect of both the driving force produced by the deformation stored

energy in the deformed austenite to produce the ferritic transformation, and the number of nucleation sites caused by the increase in the density of dislocations induced by the deformation. Therefore, the amount, rate, and temperature of deformation can have a significant effect on this type of transformation. It is observed that the deformation of the austenite at high temperatures promotes a diffusional phase transformation (also proven by the higher amount of ferrite in the HSQ&P, ≈ 41%, sample when compared to the Q&P, ≈ 21%), which leads to a higher carbon enrichment in the untransformed austenite and the decrease of the martensite start (M_s) temperature ($M_{s\text{-}Q\&P}$ = 390 ºC, $M_{s\text{-}HSQ\&P(\varepsilon=750\ ^oC)}$= 372 ºC).

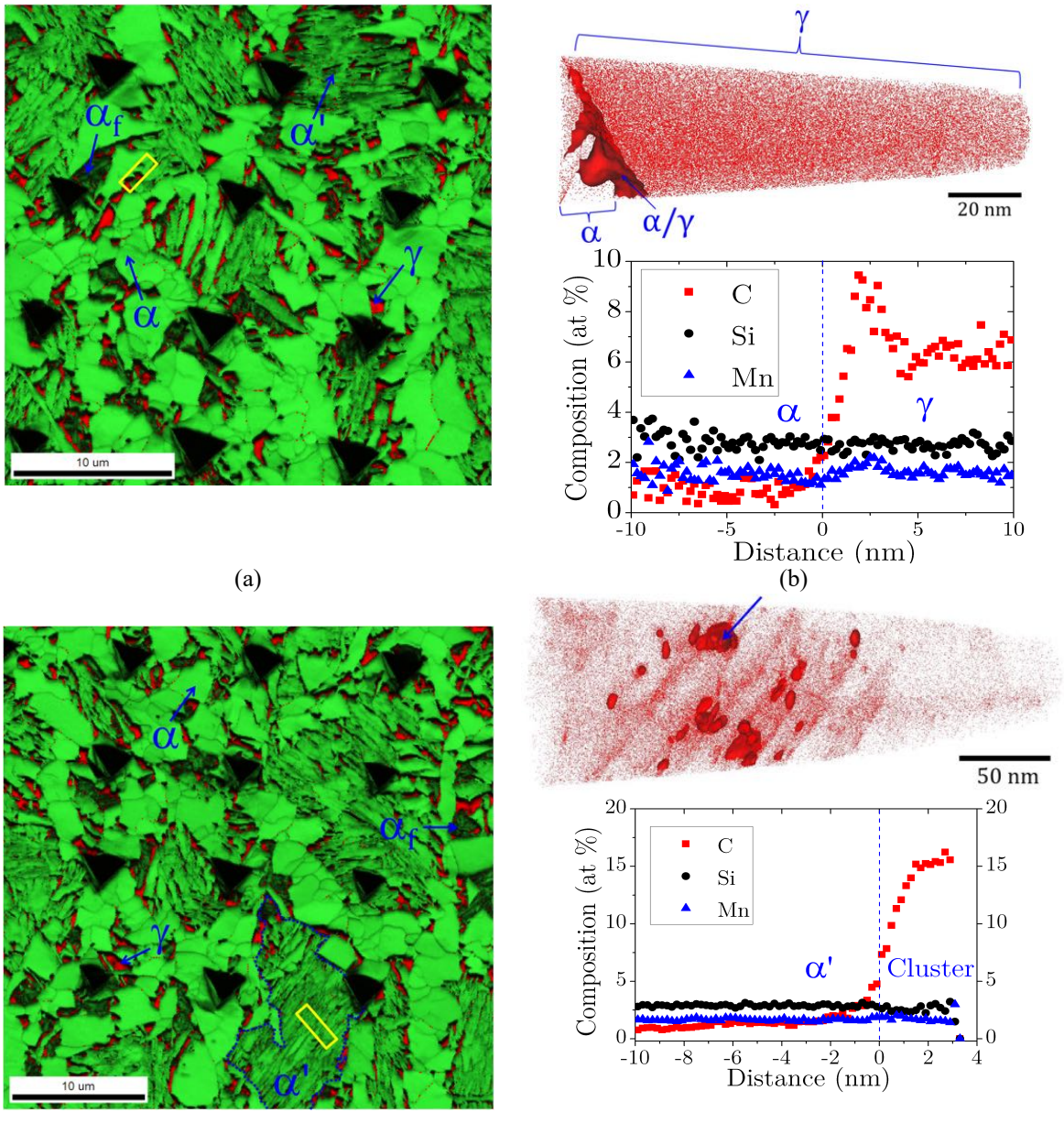

Fig. 5. Results for HSQ&P sample strained at 750 °C in 30% at a rate of 0.5 s^{-1}, quenched at 318 °C and partitioned at 400 °C for 100 s. (a) EBSD phase map of the HSQ&P_{750} sample with nanoindentations, (b) 3 at.% C isoconcentration surface for a ferrite (α) and austenite (γ) interface extracted from the region indicated in yellow rectangle in (a), and proxigrams obtained through the α/γ interface; (c) EBSD phase map of the HSQ&P_{750} sample with nanoindentations. Martensite region is delimited by blue contour; (d) carbon isoconcentration surface at 7 at.%, in the martensite region identified in the yellow rectangle in (c) and proxigrams obtained through the α'/C-cluster interface identified by the blue arrow. APT needle-shaped samples were cut from the regions highlighted by a yellow rectangles.

In Figs. 5a,c and 6 the darker green areas indicate regions with lower image quality (IQ), most likely due to a high dislocation density, and may be fresh martensite, α'_f, (martensite created during the final quench to room temperature) [55]. These areas correspond to grains containing higher densities of lattice imperfections, such as dislocations and point defects, resulting in low contrast and blurred Kikuchi bands edges, and lower quality index diffraction patterns [30]. Moreover, laths of tempered martensite may have a larger size than the fresh martensite ones, as it can transform across the whole austenite grain, while fresh martensite has to transform within smaller austenite regions after the partitioning step. Additionally, there is a greater presence of carbon-enriched retained austenite grains surrounding fresh martensite, since the latter was formed during the final quench to room temperature from the remaining austenite, which makes the distinction between fresh and tempered martensite by IQ combined with KAM map reliable. In Fig. 6, it can be observed that the high local misorientation in the fresh martensite blocks are identified by the darker green color in the image quality map, while the areas in blue (i.e., average misorientations varying between 0° and 2°) correspond to ferrite areas with higher IQ values. As can be also observed, the analyzed regions were selected from the phase map obtained by EBSD (Fig. 6). The STEM results of the regions identified with numbers 1 and 2 in Fig. 6 are shown in Figs. 7 and 8, respectively.

Fig. 7a corresponds to the surface indicated by the yellow rectangle, labeled #1, in Fig. 6 where an α'_f/α interface is identified. The appearance of carbon-enrichment in austenite (Fig. 7b) demonstrates that carbon partitioned from martensite to retained austenite during partitioning stage at 400 °C. However, if the degree of carbon enrichment in retained austenite is not sufficiently high to reduce the martensite start temperature below room temperature, part of the retained austenite transforms into fresh twinned martensite during final cooling from 400 °C to room temperature (Figs. 7c and d). The region identified as fresh martensite (α'_f) presents twin-type martensite plates (twin α'), presumably formed from carbon-enriched austenite during the final cooling. In the central part of Fig. 7, a martensite grain embedded between ferrite grains was identified. The magnification of one of the central regions of the microstructure also presents characteristics typical of twinned martensite (Fig. 7e), related to the transformation that occurs in steels with high carbon concentration. This shows that, after

the partitioning step, part of the austenite, having enough carbon to stabilize it at room temperature, remains as retained austenite, while the lower carbon content part, not completely stabilized, may transform to untempered twinned martensite.

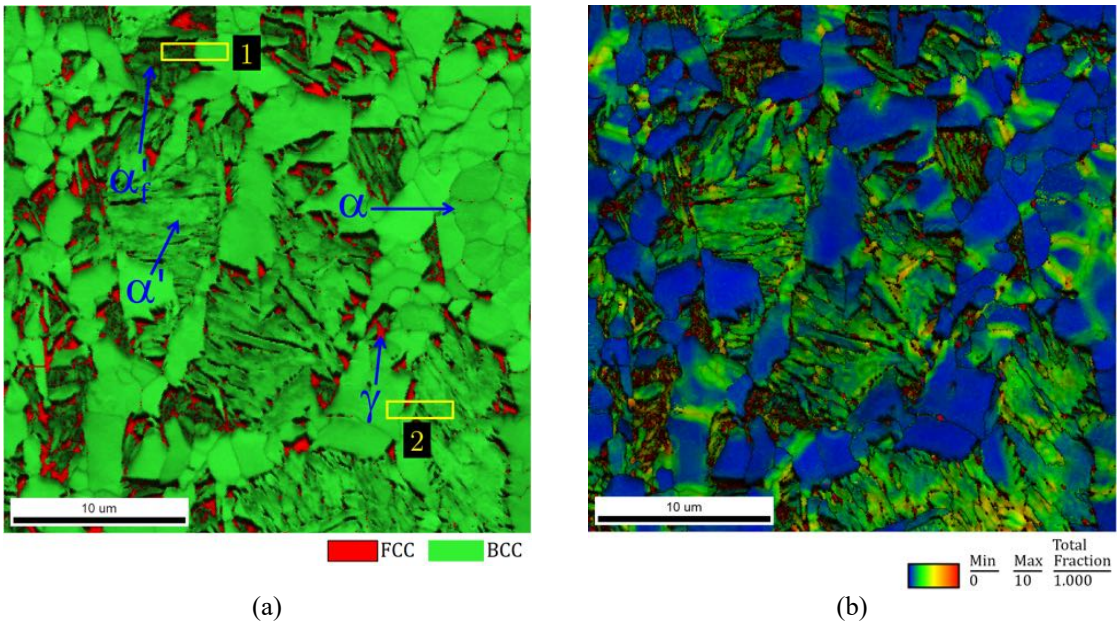

(a) (b)

Fig. 6. (a) Combined IQ map and color coded phase map identifying the regions corresponding to ferrite (α), martensite (α'), fresh martensite (α'_f), and retained austenite (γ). The distribution of γ (FCC lattice) were indicated by the red areas, while the α and α' phases (BCC lattice) appear as green. (b) Combined IQ and KAM map. HSQ&P sample strained at 750 °C in 30% at a rate of 0.5 s^{-1}, quenched at 318 °C and partitioned at 400 °C for 100 s.

The images obtained by STEM of the sample extracted from region #2 are analyzed in Fig. 8. Fig. 8a shows a bright-field (BF) STEM image of the typical interlath retained austenite (γ) with a film-like morphology (dark films) located between the martensite lath boundaries. The identification of retained austenite, ferrite and the two types of martensite: lath martensite and twin martensite (Figs. 7 and 8) is similar with previous work [57–62] also performed in steels treated by Q&P heat treatments. The presence of adjacent martensite (which formation induces defects in the surrounding austenite) and the early stage of tensile deformation during the HSQ&P process may explain this result. EDS elemental maps of carbon and manganese are shown in Figs. 8c and d. It is possible to observe that the austenite films between the laths of martensite are enriched in carbon, evidencing the partition of carbon. In addition, it is observed that carbon-enriched

austenite has a saw-tooth morphology, so that in the vicinity of the interface with ferrite the carbon enrichment is higher. This result shows that the presence of ferrite has an important role in the carbon enrichment of austenite. A possible explanation for this phenomenon is the pre-existence of a carbon accumulation in the vicinity of the original ferrite/austenite interface. The existence of this accumulation is possible if the formation of the ferrite has not reached equilibrium or if there was not enough time for the carbon to homogenize in the austenite. As the DIFT ferrite formation occurs rapidly during the straining process (duration of 0.6 s), both considerations are compatible with the experimental results. In relation to the distribution of manganese in the analyzed region (region #2), a significant accumulation of Mn along the ferrite/martensite interface (original austenite) was observed. However, it is not possible to observe a significant difference in the content of Mn in the volume (far from the interface) between martensite (austenite) and ferrite, although the partitioning of Mn can be thermodynamically predicted. This partition limited to the interface can be associated with two phenomena: the occurrence of a solute drag effect at the interface during ferrite growth, or the kinetic control regime known as local equilibrium with negligible partitioning (LENP). The LENP regimen will be discussed in the next section.

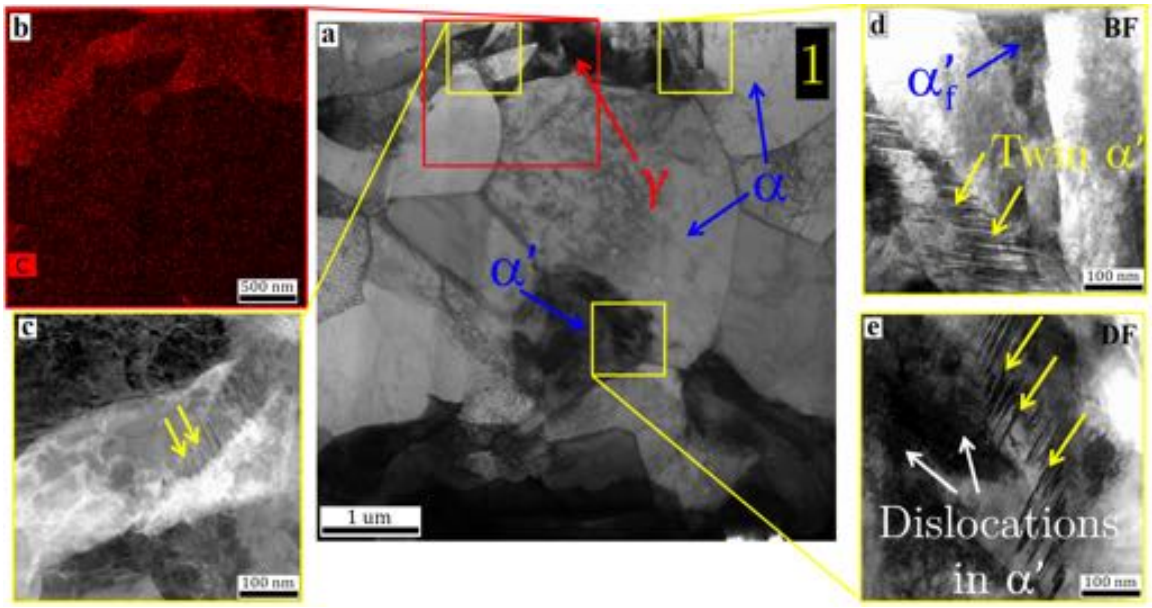

Fig. 7. (a) BF-STEM image of the region 1 identified in Fig. 6 of the HSQ&P sample strained at 750 °C in 30% at a rate of 0.5 s^{-1}, quenched at 318 °C, and partitioned at 400 °C for 100 s. (b) The carbon map (in red) obtained by energy x-ray dispersive spectroscopy (EDS). In the images with a yellow border (c-e), twinning regions are identified by the yellow arrows. (e) High angle annular dark field STEM (HAADF-STEM) image identifying. γ, α', α, and α'_f are austenita, martensite, ferrite, and fresh martensite, respectively.

The BF-STEM image of HSQ&P sample (Fig. 8) confirms the concurrence presence and stabilization of the thin films of retained austenite distributed along the carbon-depleted martensite (formed during Q&P stage). The thin-film morphology of retained austenite is expected to influence favorably on the ductility and toughness [63]. Additionally, it is known that the dislocation strengthening of the martensite is one of the important strengthening mechanisms in Q&P steels [64].

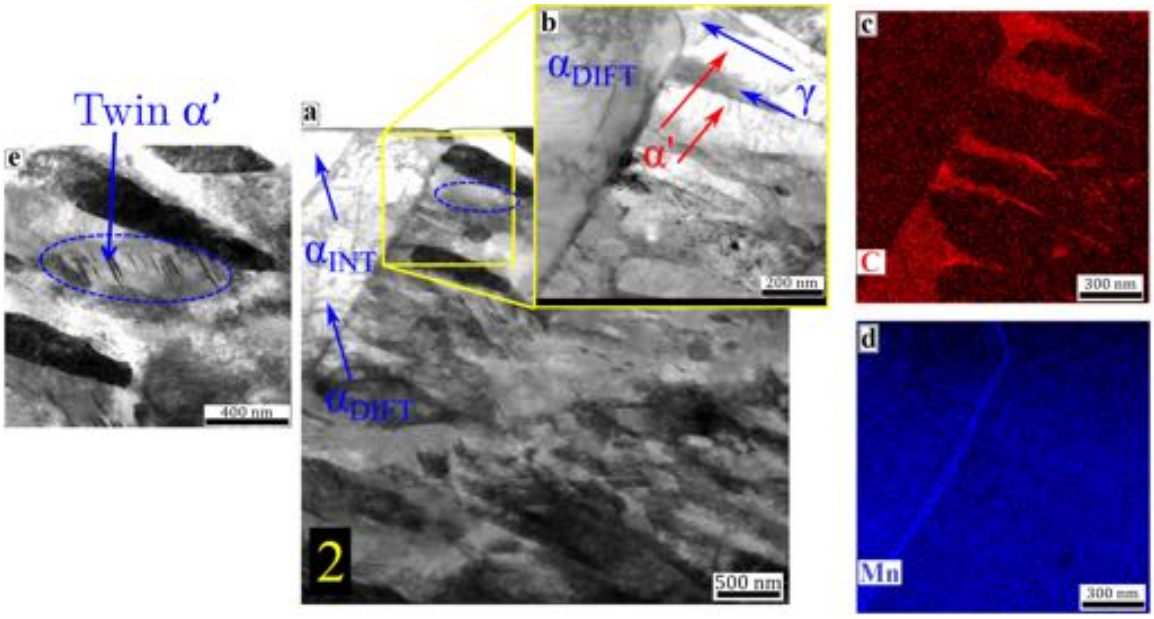

Fig. 8. (a) BF-STEM Image obtained by STEM of region 2 identified in Fig. 6 of the HSQ&P sample strained at 750 °C in 30% at a rate of 0.5 s^{-1}, quenched at 318 °C, and partitioned at 400 °C for 100 s. In the inset with the yellow border expanded (b), the bright field STEM image showing the DIFT ferrite, the lath martensite, and interlath austenite. (c-d) Corresponding EDS elemental maps of carbon (C, in red) and manganese (Mn, in blue). (e) Zoom in BF-STEM image of the region marked in blue oval in Fig. 7(a) showing twin α'. α', α_{INT}, α_{DIFT}, and γ are martensite, intercritical ferrite, DIFT ferrite, and austenite, respectively.

3.3 Characterization of the HSQ&P sample strained at 800 ºC

The APT results of the HSQ&P sample strained at 800 °C in 30% at a rate of 0.5 s^{-1}, quenched at 318 °C and partitioned at 400 °C for 100 s are shown in Fig. 9. Fig. 9a shows the EBSD phase image identifying the indentations that allowed the three regions of interest (α, ferrite, α', martensite and γ, retained austenite) to be located for APT analysis. As shown in Figs. 9a and b, the austenite evaluated in region #1 at an α'/γ interface in the vicinity of a ferrite grain is significantly enriched in carbon (Cγ ≈ 7.3 at.%), indicating that there was carbon partitioning from martensite to austenite. As previously pointed out, the carbon accumulation during the formation of DIFT ferrite may also contribute to the carbon enrichment of austenite.

At the α'/γ interface obtained in region #3 (Fig. 9d), far from the influence of the ferrite grain, carbon accumulation at the interface (Cα'/γ ≈ 7.3 at.%) was also observed; however, it is less than that observed at the interface obtained in region #1 (Cα'/γ ≈ 11

at%), as can be seen in Fig. 9b. In addition to the characterization of region #1, this result strongly indicates that the presence of ferrite in the surroundings affects the carbon content of the retained austenite (Cγ), since Cγ at the α'/γ/α interface was 7.3 at.%, while at the α'/γ interface this value was 5.9 at.%. In this figure (Fig. 9b) the proxigram obtained through an θ/α' interface is also presented. The carbon content determined at θ was ≈ 23 at.%, below the nominal composition of the cementite (25 at.%), and may be a result of artificial Carbon loss within the atom probe experiment. However, the silicon rejection observed in this carbon agglomeration region (bottom part of Fig. 9b) suggests that the identified phase is cementite (Fe_3C). Due to the high driving force for precipitation of carbides from the carbon supersaturated martensite, carbide precipitation is practically unavoidable. Thus, the partitioning of carbon from martensite to austenite and the tempering phenomenon occur simultaneously, but they are not mutually exclusive under the thermomechanical treatments carried out. Consequently, one of the main considerations of the CCE model – the absence of cementite formation during the partitioning stage – is violated.

The results of the α/γ interface analysis obtained in region #2 are shown in Fig. 9c. The measured carbon contents in γ and α in this region were ≈ 5.22 ± 0.01 at.% and ≈ 0.02 ± 0.00 at.%, respectively, while an accumulation of ≈ 6.09 ± 0.1 at.% at the interface was observed. However, although the same concentration of Mn in α and γ in the analyzed volume was observed, a high Mn enrichment at the interface was observed. As previously reported, such behavior may be associated with either a solute drag effect or ferrite growth under local equilibrium with negligible partitioning (LENP) [65]. LENP assumes that a full local equilibrium is achieved, and a very thin Mn spike is supposed to build at the α/γ interface. In order to evaluate if the width of the Mn peak is compatible with the LENP regime, Eq. (3) can be used to estimate the time required for such a peak to develop. Sun and Pugh [66] suggest that the diffusivity of manganese in austenite (D^{γ}_{Mn}) can be calculated by the expression (measured in cm^2/s):

$$D^{\gamma}_{Mn} = 0.16\, exp\left(-\frac{261700}{RT}\right) \tag{3}$$

Applying the diffusivity calculated at 800 °C and the Mn peak width estimated as 3 nm, from Eq. (3), 0.51 s it is obtained, a value close to the time interval of the deformation step in which the DIFT ferrite is formed.

The carbon enrichment of the austenite at the α/γ interface (proximity histograms in Figs. 9b and c) is produced mainly by the migration of carbon atoms coming from the ferrite growth, and in the regions far away from the interface, where there is no diffusionally enriched zone by the phase growth, the carbon content in the austenite is a consequence of the intercritical annealing condition imposed on the heat treatments. The carbon enrichment at the interfaces in both treatments (Q&P and HSQ&P) can also be explained by Fick's Law, where the diffusion flux is oriented towards a gradient of chemical composition. Therefore, if there was not this composition gradient and difference in phase solubility (in martensite the solubility of carbon is much lower and the diffusion rate is higher), the observed partitioning of carbon would not be possible. Another explanation could be the fact that grain boundaries and dislocations (the carbon atoms are trapped at dislocations present in the interface) act as sinks for carbon due to the reduction in the chemical potential of carbon at the defects (carbon segregation at the stacking faults).

In the sample submitted to the HSQ&P process with straining at 800 ºC, an increase in ferrite content of ≈ 10% was observed. This increase in DIFT ferrite (α_{DIFT}) or the strain-induced transformation (SIT) phenomenon, which is attributed to the acceleration of the nucleation rates and ferrite growth after the intercritical deformation, leads to a higher carbon content available to diffuse (since the solubility of carbon in the austenite is higher than that in the ferrite) in austenite. This behavior of the carbon redistribution also allows us to understand the presence of the twinned substructure (mainly at the interfaces) observed by transmission electron microscopy in the deformed sample, as indicated by the yellow arrows in Fig. 7. Additionally, a consequence of the higher carbon enrichment in the HSQ&P samples is that this retained austenite becomes chemically more stable due to the reduction in the martensite start (M_s) temperature, which increases the ability of the material to undergo the transformation-induced plasticity (TRIP) effect. Hence, in HSQ&P samples the carbon partitioning into austenite from supersaturated martensite, intercritical ferrite, and ferrite induced by deformation

are essential for austenite stabilization. The knowledge of these effects is essential for the understanding of the phase composition and morphology of the final microstructure and, therefore, the final properties of the material.

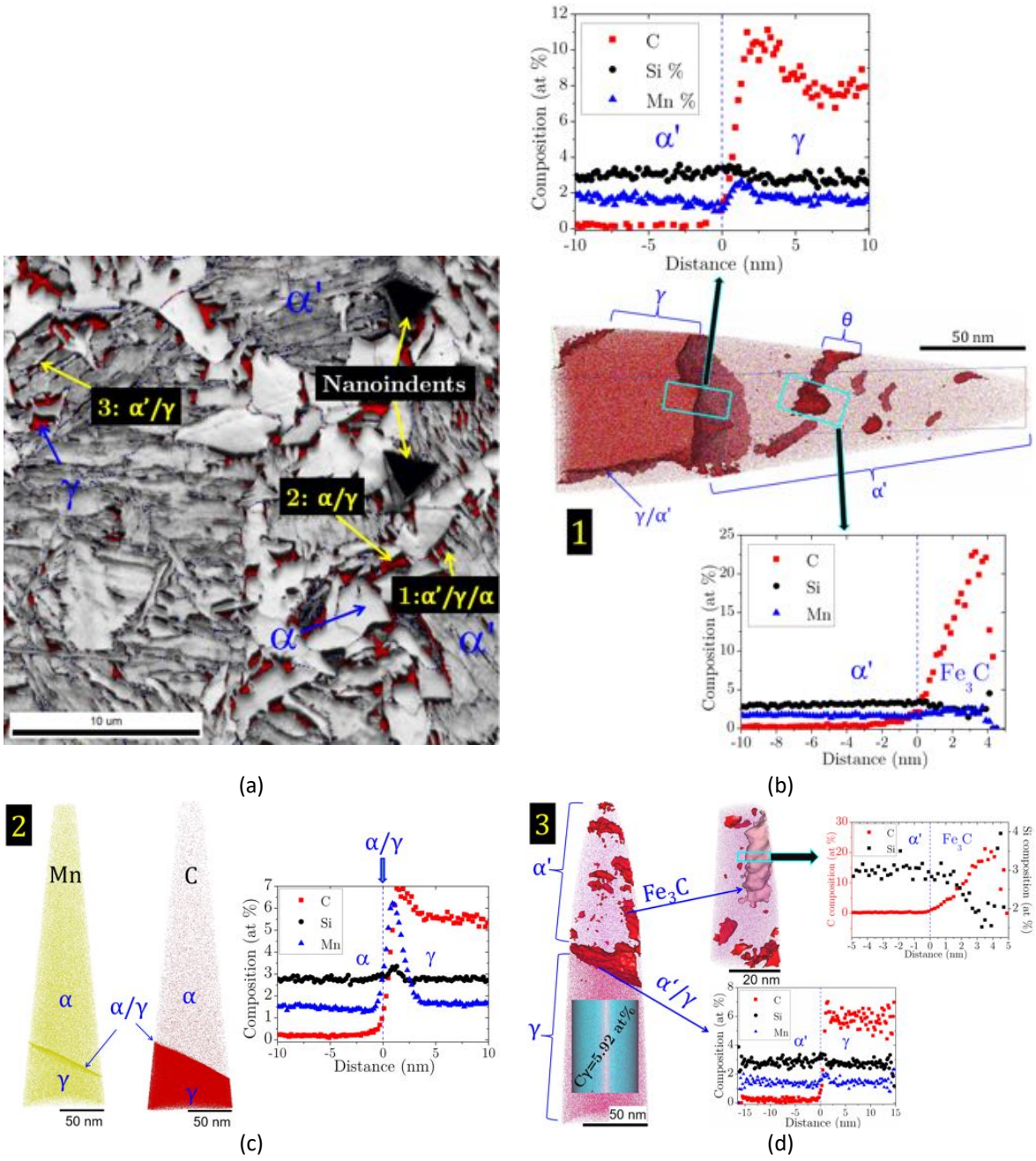

Fig. 9. HSQ&P sample strained at 800 °C in 30% at a rate of 0.5 s^{-1}, quenched at 318 °C and partitioned at 400 °C for 100 s. (a) EBSD image identifying the nanoindentations that allowed the regions of ferrite (α), martensite (α') and retained austenite (γ) to be located; (b) carbon isoconcentration surfaces at 3 at.% C,

superimposed with the carbon atom map (center), for a needle extracted from region #1, and proximity histograms obtained across α'/γ interface (top) and through a Fe_3C/α' interface (bottom). (c) Mn and C atom maps and proximity histogram across α/γ interface of the region identified as number #2 in image (a). (d) Carbon isoconcentration surface at 3 at.% C for an α'/γ interface, identified with the number #3 in image (a), superimposed with the carbon atom map, and proxigrams through a α'/Fe_3C and α'/γ interfaces.

4. Conclusions

- Due to the microstructural complexity of the samples after the Q&P and HSQ&P processes, the combined use of EBSD and nanoindentation for the identification and characterization of regions of interest for further analysis by APT and STEM proved to be very useful.
- It was possible to confirm the significant carbon enrichment of the austenite after the Q&P and HSQ&P processes, and depletion in carbon content in the martensite, which confirmed the carbon partitioning phenomenon during the partitioning step.
- The results of the Q&P sample for a film-like retained austenite indicated a percentage of carbon of 5.51 ± 0.02 at.% and 0.23 ± 0.00 at.% in martensite, with a considerable carbon accumulation at the α'/γ interface (7.6 ± 0.1 at.%). In the martensite region, precipitation of cementite was also observed.
- Blocky austenite of the Q&P sample had a carbon content of ≈ 6.00 ± 0.01 at.%. The comparison between the carbon contents of film-like inter-lath retained austenite (between martensite plates) and blocky retained austenite allowed us to confirm that the increase of the carbon content in the blocky type is due to the contribution in the carbon enrichment of both ferrite and martensite during the partition stage.
- In both Q&P and HSQ&P samples, significant carbon build-up at the interfaces was observed. Thus, the grain boundaries and dislocations may act as sinks for carbon due to the reduction in the chemical potential of carbon at defects.
- The HSQ&P samples showed the highest carbon enrichment in the austenitic phase when compared with the Q&P sample. The main reason for this higher carbon enrichment in HSQ&P samples is the contribution of the formation of proeutectoid ferrite, the

formation of DIFT ferrite, and the carbon partitioning into austenite from the supersaturated martensite, while the Q&P sample only receives a carbon contribution from the formation of proeutectoid ferrite and the martensite during the partition stage.

- A manganese concentration spike at an α'/γ interface was observed by APT and STEM. This is a strong evidence that the growth of proeutectoid ferrite occurs under local equilibrium conditions with negligible partitioning (LENP).

Acknowledgments

The authors gratefully acknowledge financial support from CAPES – (colocar o número do processo de sua bolsa), CNPq – Processes 401472/2012-4 and 235297/2014-3 – Sandwich - PhD, and FAPESP (through Grant 2014/11793-4). The Brazilian Nanotechnology National Laboratory (LNNano) and the Brazilian Synchrotron Light Laboratory (LNLS) are also acknowledged for the use of the XTMS facility at the XRD1 beamline. To Dorothy W. Coffey for FIB (Focus Ion Milling) specimen preparation. This research was performed, in part, using instrumentation (FEI Talos F200X S/TEM) provided by the Department of Energy, Office of Nuclear Energy, Fuel Cycle R&D Program and the Nuclear Science User Facilities. APT measurements were conducted at ORNL's Center for Nanophase Materials Sciences (CNMS), which is a U.S. DOE Office of Science User Facility.

References

[1] C. Wang, H. Ding, M. Cai, B. Rolfe, Multi-phase microstructure design of a novel high strength TRIP steel through experimental methodology, Mater. Sci. Eng. A. 610 (2014) 436–444. doi:10.1016/j.msea.2014.05.063.

[2] R. Blondé, E. Jimenez-Melero, L. Zhao, N. Schell, E. Brück, S. van der Zwaag, N.H. van Dijk, The mechanical stability of retained austenite in low-alloyed TRIP steel under shear loading, Mater. Sci. Eng. A. 594 (2014) 125–134. doi:10.1016/j.msea.2013.11.001.

[3] J.-C. Hell, M. Dehmas, S. Allain, J.M. Prado, A. Hazotte, J.-P. Chateau, Microstructure – Properties Relationships in Carbide-free Bainitic Steels, ISIJ Int. 51 (2011) 1724–1732. doi:10.2355/isijinternational.51.1724.

[4] Z.H. Cai, H. Ding, R.D.K. Misra, Z.Y. Ying, Austenite stability and deformation behavior in a cold-rolled transformation-induced plasticity steel with medium manganese content, Acta Mater. 84 (2015) 229–236. doi:10.1016/j.actamat.2014.10.052.

[5] P.J. Gibbs, E. De Moor, M.J. Merwin, B. Clausen, J.G. Speer, D.K. Matlock, Austenite Stability Effects on Tensile Behavior of Manganese-Enriched-Austenite Transformation-Induced Plasticity Steel, Metall. Mater. Trans. A. 42 (2011) 3691–3702. doi:10.1007/s11661-011-0687-y.

[6] E. Jimenez-Melero, N.H. van Dijk, L. Zhao, J. Sietsma, S.E. Offerman, J.P. Wright, S. van der Zwaag, Characterization of individual retained austenite grains and their stability in low-alloyed TRIP steels, Acta Mater. 55 (2007) 6713–6723. doi:10.1016/j.actamat.2007.08.040.

[7] Y. Matsuoka, T. Iwasaki, N. Nakada, T. Tsuchiyama, S. Takaki, Effect of Grain Size on Thermal and Mechanical Stability of Austenite in Metastable Austenitic Stainless Steel, ISIJ Int. 53 (2013) 1224–1230. doi:10.2355/isijinternational.53.1224.

[8] I.B. Timokhina, P.D. Hodgson, E. V. Pereloma, Effect of microstructure on the stability of retained austenite in transformation-induced-plasticity steels, Metall. Mater. Trans. A. 35 (2004) 2331–2341. doi:10.1007/s11661-006-0213-9.

[9] R. Blondé, E. Jimenez-Melero, L. Zhao, J.P. Wright, E. Brück, S. van der Zwaag, N.H. van Dijk, High-energy X-ray diffraction study on the temperature-dependent mechanical stability of retained austenite in low-alloyed TRIP steels, Acta Mater. 60 (2012) 565–577. doi:10.1016/j.actamat.2011.10.019.

[10] R. Blonde, E. Jimenez-Melero, R. Huizenga, L. Zhao, J. Wright, E. Bruck, S. van der Zwaag, N. van Dijk, High-resolution X-ray diffraction investigation on the evolution of the substructure of individual austenite grains in TRIP steels during tensile deformation, Mater. Sci. Eng. A. 47 (2014) 965–973. doi:doi:10.1107/S1600576714008553.

[11] H.L. Yi, P. Chen, H.K.D.H. Bhadeshia, Optimizing the Morphology and Stability of Retained Austenite in a δ-TRIP Steel, Metall. Mater. Trans. A. 45 (2014) 3512–3518. doi:10.1007/s11661-014-2267-4.

[12] H.S. Park, J.C. Han, N.S. Lim, C.G. Park, Nano-scale observation on the transformation behavior and mechanical stability of individual retained austenite in CMnSiAl TRIP steels, Mater. Sci. Eng. A. 627 (2015) 262–269. doi:10.1016/j.msea.2015.01.005.

[13] G. Gao, H. Zhang, X. Gui, P. Luo, Z. Tan, B. Bai, Enhanced ductility and toughness in an ultrahigh-strength Mn–Si–Cr–C steel: The great potential of ultrafine filmy retained austenite, Acta Mater. 76 (2014) 425–433. doi:10.1016/j.actamat.2014.05.055.

[14] Y.F. Shen, Y.D. Liu, X. Sun, Y.D. Wang, L. Zuo, R.D.K. Misra, Improved ductility of a transformation-induced-plasticity steel by nanoscale austenite lamellae, Mater. Sci. Eng. A. 583 (2013) 1–10. doi:10.1016/j.msea.2013.06.062.

[15] X.C. Xiong, B. Chen, M.X. Huang, J.F. Wang, L. Wang, The effect of morphology on the stability of retained austenite in a quenched and partitioned steel, Scr. Mater. 68 (2013) 321–324. doi:10.1016/j.scriptamat.2012.11.003.

[16] N. Nakada, Y. Ishibashi, T. Tsuchiyama, S. Takaki, Self-stabilization of untransformed austenite by hydrostatic pressure via martensitic transformation, Acta Mater. 110 (2016) 95–102. doi:10.1016/j.actamat.2016.03.048.

[17] J. Speer, D.K. Matlock, B.C. De Cooman, J.G. Schroth, Carbon partitioning into austenite after martensite transformation, Acta Mater. 51 (2003) 2611–2622. doi:10.1016/S1359-6454(03)00059-4.

[18] A.J. Clarke, J.G. Speer, M.K. Miller, R.E. Hackenberg, D.V. Edmonds, D.K. Matlock, F.C. Rizzo, K.D. Clarke, E. De Moor, Carbon partitioning to austenite from martensite or bainite during the quench and partition (Q&P) process: A critical assessment, Acta Mater. 56 (2008) 16–22. doi:10.1016/j.actamat.2007.08.051.

[19] G. a. Thomas, J.G. Speer, D.K. Matlock, Quenched and Partitioned Microstructures Produced via Gleeble Simulations of Hot-Strip Mill Cooling Practices, Metall. Mater. Trans. A. 42 (2011) 3652–3659. doi:10.1007/s11661-011-

0648-5.

[20] S. Kim, J. Lee, F. Barlat, M.G. Lee, Transformation kinetics and density models of quenching and partitioning (Q&P) steels, Acta Mater. 109 (2016) 394–404. doi:10.1016/j.actamat.2015.11.051.

[21] F. HajyAkbary, J. Sietsma, G. Miyamoto, T. Furuhara, M.J. Santofimia, Interaction of carbon partitioning, carbide precipitation and bainite formation during the Q&P process in a low C steel, Acta Mater. 104 (2016) 72–83. doi:10.1016/j.actamat.2015.11.032.

[22] E.J. Seo, L. Cho, B.C. De Cooman, Kinetics of the partitioning of carbon and substitutional alloying elements during quenching and partitioning (Q &P) processing of medium Mn steel, Acta Mater. 107 (2016) 354–365. doi:10.1016/j.actamat.2016.01.059.

[23] Y. Toji, G. Miyamoto, D. Raabe, Carbon partitioning during quenching and partitioning heat treatment accompanied by carbide precipitation, Acta Mater. 86 (2015) 137–147. doi:10.1016/j.actamat.2014.11.049.

[24] D.T. Pierce, D.R. Coughlin, D.L. Williamson, K.D. Clarke, a J. Clarke, J.G. Speer, Characterization of transition carbides in quench and partitioned steel microstructures by Mössbauer spectroscopy and complementary techniques, Acta Mater. 90 (2015) 1–14. doi:10.1016/j.actamat.2015.01.024.

[25] H. Liu, H. Sun, B. Liu, D. Li, F. Sun, X. Jin, An ultrahigh strength steel with ultrafine-grained microstructure produced through intercritical deformation and partitioning process, Mater. Des. 83 (2015) 760–767. doi:10.1016/j.matdes.2015.06.047.

[26] M. Karam-Abian, A. Zarei-Hanzaki, H.R. Abedi, S. Heshmati-Manesh, Micro and macro-mechanical behavior of a transformation-induced plasticity steel developed by thermomechanical processing followed by quenching and partitioning, Mater. Sci. Eng. A. 651 (2016) 233–240. doi:10.1016/j.msea.2015.10.116.

[27] Y. Chang, G. Li, C. Wang, X. Li, H. Dong, Effect of Quenching and Partitioning with Hot Stamping on Martensite Transformation and Mechanical Properties of AHSS, J. Mater. Eng. Perform. 24 (2015) 3194–3200. doi:10.1007/s11665-015-1579-x.

[28] H. Liu, X. Lu, X. Jin, H. Dong, J. Shi, Enhanced mechanical properties of a hot stamped advanced high-strength steel treated by quenching and partitioning process, Scr. Mater. 64 (2011) 749–752. doi:10.1016/j.scriptamat.2010.12.037.

[29] H. Liu, X. Jin, H. Dong, J. Shi, Martensitic microstructural transformations from the hot stamping, quenching and partitioning process, Mater. Charact. 62 (2011) 223–227. doi:10.1016/j.matchar.2010.12.003.

[30] E.A. Ariza, A.S. Nishikawa, H. Goldenstein, A.P. Tschiptschin, Characterization and methodology for calculating the mechanical properties of a TRIP-steel submitted to hot stamping and quenching and partitioning (Q&P), Mater. Sci. Eng. A. 671 (2016) 54–69. doi:10.1016/j.msea.2016.06.038.

[31] D. De Knijf, R. Petrov, C. Föjer, L.A.I. Kestens, Effect of fresh martensite on the stability of retained austenite in quenching and partitioning steel, Mater. Sci. Eng. A. 615 (2014) 107–115.

[32] E.J. Seo, L. Cho, B.C. De Cooman, Acta Materialia Kinetics of the partitioning of carbon and substitutional alloying elements during quenching and partitioning (Q & P) processing of medium Mn steel, Acta Mater. 107 (2016) 354–365. doi:10.1016/j.actamat.2016.01.059.

[33] G.A. Thomas, F. Danoix, J.G. Speer, S.W. Thompson, F. Cuvilly, Carbon Atom Re-Distribution during Quenching and Partitioning, ISIJ Int. 54 (2014) 2900–2906.

[34] Y. Toji, H. Matsuda, M. Herbig, P.-P. Choi, D. Raabe, Atomic-scale analysis of carbon partitioning between martensite and austenite by atom probe tomography and correlative transmission electron microscopy, Acta Mater. 65 (2014) 215–228. doi:10.1016/j.actamat.2013.10.064.

[35] H. Dong, X. Sun, Deformation induced ferrite transformation in low carbon steels, Curr. Opin. Solid State Mater. Sci. 9 (2005) 269–276. doi:10.1016/j.cossms.2006.02.014.

[36] C. Ghosh, V. V. Basabe, J.J. Jonas, Y.M. Kim, I.H. Jung, S. Yue, The dynamic transformation of deformed austenite at temperatures above the Ae3, Acta Mater. 61 (2013) 2348–2362. doi:10.1016/j.actamat.2013.01.006.

[37] A. Bardelcik, M.J. Worswick, M.A. Wells, The influence of martensite , bainite and ferrite on the as-quenched constitutive response of simultaneously quenched

and deformed boron steel – Experiments and model, 55 (2014) 509–525.

[38] J. Wu, P.. Wray, C.. Garcia, M. Hua, A.. Deardo, Image quality analysis: A new method of characterizing microstructures, ISIJ Int. 45 (2005) 254–262. doi:10.2355/isijinternational.45.254.

[39] K. Radwanski, Structural characterization of low-carbon multiphase steels merging advanced research methods with light optical microscopy, Arch. Civ. Mech. Eng. 16 (2016) 282–293. doi:10.1016/j.acme.2015.12.001.

[40] L. Yuan, Nanoscale austenite reversion through partitioning , segregation and kinetic freezing in martensitic stainless steels, Max-Planck-Institute fur Eisenforschung, 2012.

[41] R. Petrov, L. Kestens, A. Wasilkowska, Y. Houbaert, Microstructure and texture of a lightly deformed TRIP-assisted steel characterized by means of the EBSD technique, Mater. Sci. Eng. A. 447 (2007) 285–297. doi:10.1016/j.msea.2006.10.023.

[42] G. Thomas, J. Speer, D. Matlock, J. Michael, Application of electron backscatter diffraction techniques to quenched and partitioned steels., Microsc. Microanal. 17 (2011) 368–373. doi:10.1017/S1431927610094432.

[43] D. De Knijf, R. Petrov, C. Föjer, L.A.I. Kestens, Effect of fresh martensite on the stability of retained austenite in quenching and partitioning steel, Mater. Sci. Eng. A. 615 (2014) 107–115. doi:10.1016/j.msea.2014.07.054.

[44] K. Thompson, D. Lawrence, D.J. Larson, J.D. Olson, T.F. Kelly, B. Gorman, In situ site-specific specimen preparation for atom probe tomography, Ultramicroscopy. 107 (2007) 131–139. doi:10.1016/j.ultramic.2006.06.008.

[45] F.A.-F. W. Poling, V. Savic, L.G. Hector, Jr., A.K. Sachdev, X. Hu, A. Devaraj, X. Sun, Combined Synchrotron X-Ray Diffraction and Digital Image Correlation Technique for Measurement of Austenite Transformation with Strain in TRIP-Assisted Steels, SAE Int. (2016) 1–5.

[46] D. De Knijf, R. Petrov, C. Föjer, L.A.I. Kestens, Effect of fresh martensite on the stability of retained austenite in quenching and partitioning steel, Mater. Sci. Eng. A. 615 (2014) 107–115. doi:10.1016/j.msea.2014.07.054.

[47] M.J. Santofimia, L. Zhao, J. Sietsma, Microstructural Evolution of a Low-Carbon

Steel during Application of Quenching and Partitioning Heat Treatments after Partial Austenitization, Metall. Mater. Trans. A. 40 (2008) 46–57. doi:10.1007/s11661-008-9701-4.

[48] I.B. Timokhina, H. Beladi, X.Y. Xiong, Y. Adachi, P.D. Hodgson, Nanoscale microstructural characterization of a nanobainitic steel, Acta Mater. 59 (2011) 5511–5522. doi:10.1016/j.actamat.2011.05.024.

[49] I.B. Timokhina, E. V. Pereloma, S.P. Ringer, R.K. Zheng, P.D. Hodgson, Characterization of the Bake-hardening Behavior of Transformation Induced Plasticity and Dual-phase Steels Using Advanced Analytical Techniques, ISIJ Int. 50 (2010) 574–582. doi:10.2355/isijinternational.50.574.

[50] B. Hutchinson, J. Hagström, O. Karlsson, D. Lindell, M. Tornberg, F. Lindberg, M. Thuvander, Microstructures and hardness of as-quenched martensites (0.1–0.5%C), Acta Mater. 59 (2011) 5845–5858. doi:10.1016/j.actamat.2011.05.061.

[51] H. Qu, Advanced High Strength Steel through Paraequilibrium Carbon Partitioning and Austenite Stabilization, Case Western Reserve University, 2013.

[52] K. Hase, C. Garcia-Mateo, H.K.D.H. Bhadeshia, Bainite formation influenced by large stress, Mater. Sci. Technol. 20 (2004) 1499–1505. doi:10.1179/026708304X6130.

[53] H.K.D.H. Bhadeshia, Stress and Strain Effects, in: Bainite in Steels, 2nd ed., London, 2001: pp. 201–224.

[54] A. Mohamadizadeh, A. Zarei-Hanzaki, S. Heshmati-Manesh, A. Imandoust, The effect of strain induced ferrite transformation on the microstructural evolutions and mechanical properties of a TRIP-assisted steel, Mater. Sci. Eng. A. 607 (2014) 621–629. doi:http://dx.doi.org/10.1016/j.msea.2014.04.044.

[55] M.J. Santofimia, L. Zhao, J. Sietsma, Microstructural Evolution of a Low-Carbon Steel during Application of Quenching and Partitioning Heat Treatments after Partial Austenitization, Metall. Mater. Trans. A. 40 (2008) 46–57. doi:10.1007/s11661-008-9701-4.

[56] J. Chen, K. Sand, M.S. Xia, C. Ophus, R. Mohammadi, M.L. Kuntz, Y. Zhou, D. Mitlin, Transmission Electron Microscopy and Nanoindentation Study of the Weld Zone Microstructure of Diode-Laser-Joined Automotive Transformation-Induced

Plasticity Steel, Metall. Mater. Trans. A. 39 (2008) 593–603. doi:10.1007/s11661-007-9389-x.

[57] J. Sun, H. Yu, Microstructure development and mechanical properties of quenching and partitioning (Q&P) steel and an incorporation of hot-dipping galvanization during Q&P process, Mater. Sci. Eng. A. 586 (2013) 100–107. doi:10.1016/j.msea.2013.08.021.

[58] N. Maheswari, S.G. Chowdhury, K.C.H. Kumar, S. Sankaran, Influence of alloying elements on the microstructure evolution and mechanical properties in quenched and partitioned steels, Mater. Sci. Eng. A. 600 (2014) 12–20. doi:10.1016/j.msea.2014.01.066.

[59] E.J. Seo, L. Cho, B.C. De Cooman, Application of quenching and partitioning (Q&P) processing to press hardening steel, Metall. Mater. Trans. A Phys. Metall. Mater. Sci. 45 (2014) 4022–4037. doi:10.1007/s11661-014-2316-z.

[60] C. Song, H. Yu, L. Li, T. Zhou, J. Lu, X. Liu, The stability of retained austenite at different locations during straining of I&Q&P steel, Mater. Sci. Eng. A. 670 (2016) 326–334. doi:10.1016/j.msea.2016.06.044.

[61] J. Dong, X. Zhou, Y. Liu, C. Li, C. Liu, H. Li, Effects of quenching-partitioning-tempering treatment on microstructure and mechanical performance of Nb-V-Ti microalloyed ultra-high strength steel, Mater. Sci. Eng. A. 690 (2017) 283–293. doi:10.1016/j.msea.2017.03.020.

[62] W. Li, H. Gao, H. Nakashima, S. Hata, W. Tian, Microstructural evolution and mechanical properties of a low-carbon quenching and partitioning steel after partial and full austenitization, Int. J. Miner. Metall. Mater. 23 (2016) 906–919. doi:10.1007/s12613-016-1306-0.

[63] W.T. Zhao, X.F. Huang, W.G. Huang, Comparative study on a 0.2C steel treated by Q&P and A&T treatments, Mater. Sci. Technol. 32 (2016) 1–8. doi:10.1080/02670836.2015.1126049.

[64] H.R. Ghazvinloo, A. Honarbakhsh-Raouf, E. Borhani, Morphological Characteristics of Retained Austenite in 0.362C–1.38Si–1.24Mn Steel Processed by One-Step Quenching and Partitioning, Metallurgist. 60 (2016) 758–764. doi:10.1007/s11015-016-0363-y.

[65] M. Gouné, F. Danoix, J. Ågren, Y. Bréchet, C.R. Hutchinson, M. Militzer, G. Purdy, S. van der Zwaag, H. Zurob, Overview of the current issues in austenite to ferrite transformation and the role of migrating interfaces therein for low alloyed steels, Mater. Sci. Eng. R Reports. 92 (2015) 1–38. doi:10.1016/j.mser.2015.03.001.

[66] S. Sun, M. Pugh, Manganese Partitioning in Dual-Phase Steel During Annealing, Mater. Sci. Eng. A. 276 (2000) 167–174. doi:10.1016/S0921-5093(99)00261-0.